How Hot Plasmonic Heating Can Be: Phase Transition and Melting of P25 TiO_2 from Plasmonic Heating of Au Nanoparticles

Weigang Lu[1§], Rohil Kayastha[1§], Blake Birmingham[1], Bernd Zechmann[2], Zhenrong Zhang[1*]

1- Department of Physics, Baylor University, Waco, Texas 76798, United States

2- Center for Microscopy and Imaging, Baylor University, Waco, Texas 76798, United States

[*]Email: Zhenrong_Zhang@baylor.edu

[§]W.L. and R.K. contributed equally to this paper.

Abstract:

Plasmonic heating has been utilized in many applications, including photocatalysis, photothermal therapy, and photocuring. However, the heat dissipation process of the plasmonic nanoparticles (NPs) and the surrounding matrix is complex. How high the temperature of the matrix that surrounds the plasmonic NPs, such as the catalyst and substrate, can be reached is unclear. Herein, we study the dissipation of plasmonic heat generated by resonantly excited gold (Au) NPs dispersed on P25 TiO_2 NP porous film in air. Under resonant 532 nm continuous wave (CW) laser irradiation at the surface of the Au-TiO_2, the surface evaporation and the aggregation of Au NPs were observed at moderate laser power (10 mW/um^2). This process is accompanied by the phase transition of TiO_2. More importantly, the TiO_2 nanoparticle film melted, forming melt pools and molten TiO_2 matrix. This indicates that the temperature of the TiO_2 reached as high as its melting point of 1830 °C. When Au/TiO_2 was irradiated with an off-resonance laser at 638 nm, no phase

transformation or melting of TiO_2 was observed. The temperature calculation showed that the heating generated by Au NPs is not localized. The collective heating from an ensemble of Au NPs in the irradiated area produced a global temperature rise that melted TiO_2. Our results suggest that the photothermal effect could be a significant mechanism in the plasmon-assisted photocatalytic reactions. The melting of the supporting metal oxide film by plasmonic heating at relatively low laser power suggests new applications for utilizing plasmonic heating, such as additive manufacturing.

Keywords: Localized surface plasmons, Laser plasmonic heating, Phase transition, TiO_2 melting, Additive manufacturing

Plasmonic heating has been utilized in various applications such as photothermal catalysis,[1-4] water evaporation,[5, 6] photothermal therapy,[7-9] and epoxy photocuring.[10] Localized surface plasmon resonance (LSPR) is the phenomenon when oscillations of the conduction electrons of metallic nanoparticles (NPs) are at resonance with the oscillations of the electromagnetic field of the incident light, which significantly increases the absorption of the incoming light at the resonant frequencies.[1, 11-13] The heat generated from plasmonic NPs elevates the temperature of the NPs, the surrounding media like air, water, and the supporting matrix including substrate or catalyst.[1, 11, 14-18] It has been shown that plasmonic heating can reach the melting temperature of plasmonic ZrN NPs.[19] Deformation of the glass substrate was also observed due to the melting and evaporation of Au NPs supported on a glass substrate.[20] However, the impact and the mechanism of plasmonic heating on the morphology and structure of the supporting matrix are scarcely studied. In addition, there is a discrepancy between the experimentally observed particle temperature and surrounding media and the temperature calculated *via* a single

particle model. For example, water boiling was experimentally observed when the plasmonic Au nanoparticle solution was illuminated by solar light; however, the calculated increase in temperature of the Au nanoparticle was as tiny as 0.04 °C with the conventional macroscopic model. A thermal barrier between NPs-vapor bubble interface was proposed to address the high vaporization efficiency.[21]

Recently, the role of collective heating in plasmonic heating has regained attention due to the difficulty in distinguishing thermal and non-thermal contributions in plasmon-driven processes.[22-24] Keblinski *et al.* have proposed two contributions to plasmonic heating: self-heating and collective heating.[25] Although most of the materials experience temperature increases due to light absorption, plasmonic self-heating refers to the temperature increase of the well-separated NPs with the increased absorption cross-section of the light at the plasmonic resonance. The resonance photoexcitation generates hot electron-hole pairs. The relaxation of the excited hot charge carriers *via* electron-electron and electro-phonon scattering increases the temperature of the plasmonic particles and the surrounding media.[1, 11] Collective heating or global heating is the heating provided by all the plasmonic particles in the irradiated region to the individual localized particles. Theoretical calculations showed that collective heating could increase the temperature by orders of magnitude higher for the plasmonic nanoparticle assemblies than for the single particles.[25,15, 24] However, the associated temperature increase was often difficult to predict. Whether the temperature was confined to the vicinity of the NPs or delocalized was related to the spatial distribution of the NPs. The time scale of the temperature increases and heat dissipation in thermodynamics was also challenging to estimate because of the nonuniformity of the surroundings. Additionally, the temperature of the NPs was difficult to measure.[24] Most of the temperature microscopy methods utilize optical spectroscopy. Although the melting of the

plasmonic materials and the support and the surface evaporation of plasmonic materials have been observed, the experimentally obtained melting temperature was much lower than the high temperature (thousands of Kevin) predicted.[19, 20, 26]

Since 2010, plasmonic chemistry has become an attractive approach to enhance the photoreactivity of the catalysts.[12, 27, 28] For example, plasmonic gold NPs supported on titanium dioxide (TiO_2) are widely reported to have better photocatalytic performance than pristine TiO_2 systems.[28-30] The primary mechanism of plasmon-assisted photoreactivity has long been connected to hot carriers. Recently, alternative mechanisms, such as photothermal effects and enhanced near field, have been proposed to make a significant contribution.[24, 31-34] Theoretical studies suggest that the photothermal effect can explain the observed enhanced photocatalytic reactivity.[35-37] However, little experimental evidence showed the contribution of plasmonic heating because of the difficulty of measuring the temperature and separating plasmonic heating from other mechanisms.[24]

Degussa P25, composed of anatase and rutile nanocrystallites, is the golden standard for the TiO_2 photocatalyst. Among TiO_2 polymorphs, anatase is the metastable phase, whereas rutile is the stable polymorph under ambient conditions. Anatase-rutile phase transition (ART) occurs at a wide temperature range between 400 °C and 1200 °C.[38-40] Laser-induced phase transition has been reported using femtosecond laser,[41] and nanosecond UV laser[42]. Anatase NPs transformed into an amorphous phase,[43] or rutile phase,[44] depending on the laser and the surrounding matrix. Plasmonic heating enabled the local phase transition of amorphous TiO_2 thin film into the anatase phase, observed on polymetric beads coated with Au thin film by a low-power CW laser irradiation.[45] Here, the plasmonic heating alone did not introduce phase transition. The heat was attributed to the plasmonic heating, which was enhanced by the exothermic decomposition of the

polymetric beads. In general, the melting of the surrounding media with a melting point as high as ~1800 °C has not been reported from plasmonic heating by a CW laser.

In this work, we studied the impact of the plasmonic heating generated by Au NPs on the surrounding photocatalyst support, specifically, TiO_2 (Degussa P25) nanoparticle thin film. We investigated phase transition and melting of TiO_2 nanoparticle thin film and surface evaporation of Au under different laser powers on and off the plasmonic resonance. The temperature of Au and TiO_2 NPs was compared with the calculated temperature using the established theoretical model by considering self-heating and collective heating. The temperature was also directly measured using Raman spectroscopy. The results raised questions about the high transient temperature that the Au and TiO_2 experienced in the photocatalytic reactions.

Results and discussions:

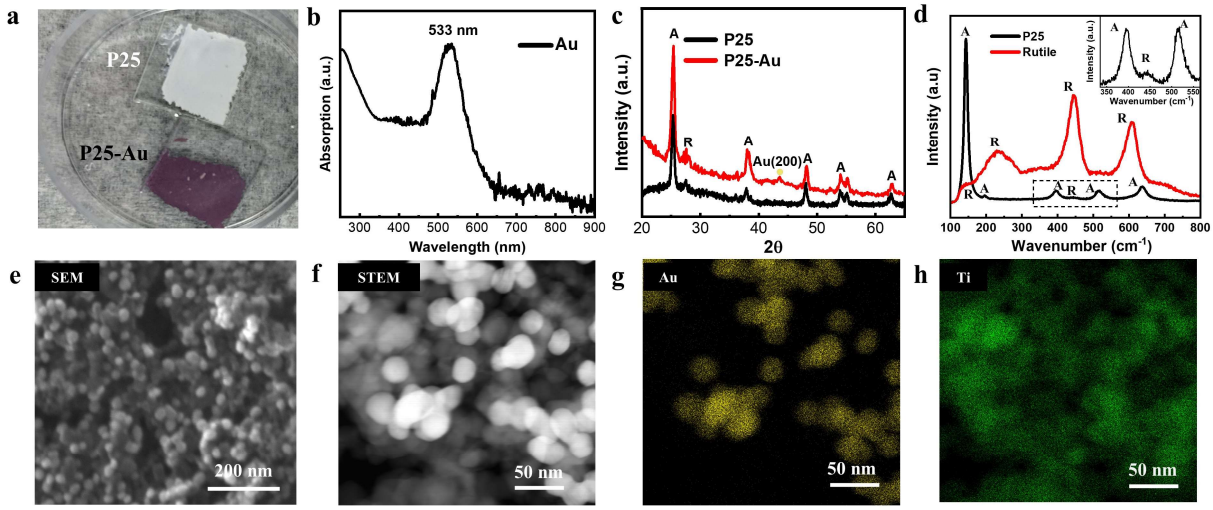

Figure 1: Characterization of the P25 TiO_2 film and Au-decorated P25 TiO_2 film. **a)** Optical image of the samples on the glass slide: P25 and P25-Au. **b)** UV-Vis of the Au NPs with resonance at

533 nm. **c)** XRD of the P25 and P25-Au. **d)** Raman spectra of the P25 sample and a rutile TiO_2(110) bulk crystal. The inset shows the zoomed-in spectra of the P25 in a black dashed box. **e)** SEM image of P25-Au film showing a mixture of P25 (darker particles) and Au NPs (brighter particles). **f)** HAADF-STEM image of the P25-Au NPs. EDS map of the image displayed in f) showing **g)** Au NPs and **h)** Ti element of the P25 (TiO_2). **Labels:** R: Rutile, A: Anatase, and Au: Gold

P25 film, consisting of anatase and rutile TiO_2 NPs, was used as a support to test the effects of plasmonic heating in this study. The sample preparation and characterization are described in the Methods section. After the Au NPs decorated the P25 film, the white P25 sample turned to darker red (**Figure 1a)**. The LSPR absorption of the Au nanoparticle was at 533 nm **(Figure 1b),** thus, the reflection of a rich red color was observed.[46] The 532 nm wavelength laser source was chosen for maximum resonance absorption in the plasmonic heating study. The size of the Au NPs was around 25-30 nm (**Figure S1**). The average size of the P25 NPs was around 27 nm, measured from the TEM images. XRD patterns (**Figure 1c**) of P25 and P25-Au thin films match the characteristic patterns of P25 and FCC gold NPs.[47-52] The P25 was a mixer of anatase nanocrystals (~80%) and rutile nanocrystals (15%); thus, anatase and rutile peaks were observed in the XRD. The crystal structure of the TiO_2 NPs was measured using Raman spectroscopy. The Raman spectra of the P25 and the rutile phase of TiO_2 (**Figure 1d)** matched the reference spectra from previous reports.[53-55] The Raman spectrum of P25 exhibits a combination of anatase and rutile peaks (**Figure 1d** black curve**)**. The peaks of the anatase vibrational spectrum can be observed at 143 cm^{-1} (E_g mode), 195 cm^{-1} (E_g mode), 396 cm^{-1} (B_{1g} mode), 517 cm^{-1} (A_{1g} mode), and 638 cm^{-1} (E_g mode),[52, 56-61] and the rutile E_g mode of 446 cm^{-1} as shown in the insertion. The rutile peaks (**Figure 1d** red curve) at 143, 446, and 608 cm^{-1} are assigned to the B_{1g}, E_g, and A_{1g} symmetric

modes, respectively.[53, 60-62] The broad peak at 239 cm^{-1} was associated with the disorder-induced scattering or second-order effect in the rutile spectra.[61 53, 63]

When the Au NPs were attached to the P25 thin film, the SEM image **(Figure 1e)** showed that the Au NPs were distributed uniformly but randomly on the TiO_2 porous film. Here, the Au and P25 NPs correspond to the brighter and darker particles. The estimated Au nanoparticle density from SEM images was about 600/μm^2 **(Figure S2)**. The elemental composition image of the P25-Au film was obtained using the HAADF-STEM (**Figure 1f),** showing the composition of the P25-Au mixture**.** The elemental composition from the EDS map verified that the actual particles, Au (**Figure 1g**) and Ti (**Figure 1h),** from TiO_2 NPs present in the mixture match the spatial distribution of TiO_2 and Au NPs from the HAADF image.

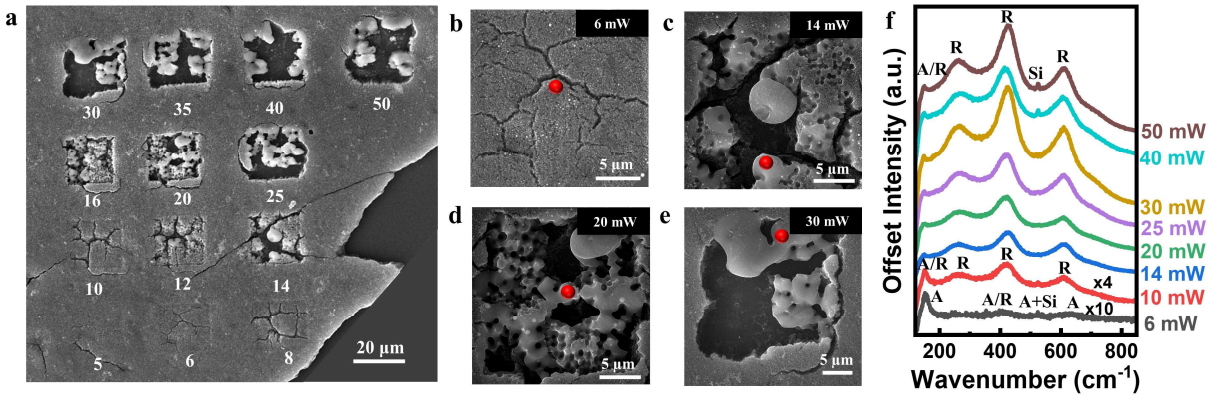

Figure 2: Characterization of the P25-Au film after on-resonance laser irradiation. **a)** SEM image of Au-decorated P25 film after irradiation with 532 nm CW laser at different laser powers. The white colored numbers correspond to laser power in milliwatts (mW). Zoomed-in SEM images for the areas experienced various laser powers: **b)** 6 mW, **c)** 14 mW, **d)** 20 mW, and **e)** 30 mW. Raman spectra of different spots marked as red dots in **b)** to **e)** are shown in **f)** along with other scanned areas at various laser powers. **Labels:** R: Rutile, A: Anatase, and Si: Silicon. The 6 mW and 10 mW

Raman spectra intensity were multiplied by 10 and 4 times, respectively, to compare with the other spectra.

The impact of plasmonic heating with a 532 nm laser source on the morphology and structure of the P25-Au sample is presented in **Figure 2**. The P25-Au film on silicon substrate was irradiated by scanning a 20 × 20 μm^2 area with the laser beam with a 500 ms exposure. The Raman map of the area was simultaneously collected during the scan. The SEM image (**Figure 2a**) of the P25-Au surface after laser irradiation with various increasing laser power shows that the heat generated during the scan causes dramatic changes in the morphology of the scan areas. At lower power (6 mW), cracks formed on the surface (**Figure 2b**). As the laser power increased, the size and depth of the cracks became more extensive (Figure 2a), and the formation of holes/melted pools and molten balls of TiO_2 was also observed (**Figures 2c-2d**). The Raman spectrum (**Figure 2f**) at 6 mW power showed that the P25 remained almost unchanged (black curve **Figure 1d**). The P25 nanocrystal structure was gradually transformed from mainly anatase to mainly rutile phase as more rutile peaks were observed (**Figure 2f**). In addition to the ART phase transition, agglomerations of melted TiO_2 were seen at higher power (>12 mW, **Figures 2c-2e**). The exposed area of the Si surface also increased as the melted TiO_2 and Au NPs aggregated together **(Figure S5)**. For comparison, the sintering of P25 and P25-Au films on Si substrate was carried out separately in a muffle oven. No indication of melting was observed after annealing to 1080 °C (**Figure S3**), which is expected from the melting temperature of TiO_2 NPs. XRD showed that P25 anatase-rutile transition occurred between 600ºC to 700ºC **(Figure S4a)**, consistent with the reported P25 phase transition.[64-67] The results suggest that as high as the melting temperature (~1830°C) of the TiO_2 NPs was reached due to the dissipation of the plasmonic heating as the laser

power increased. More details on these effects of plasmonic heating are explained in the later section.

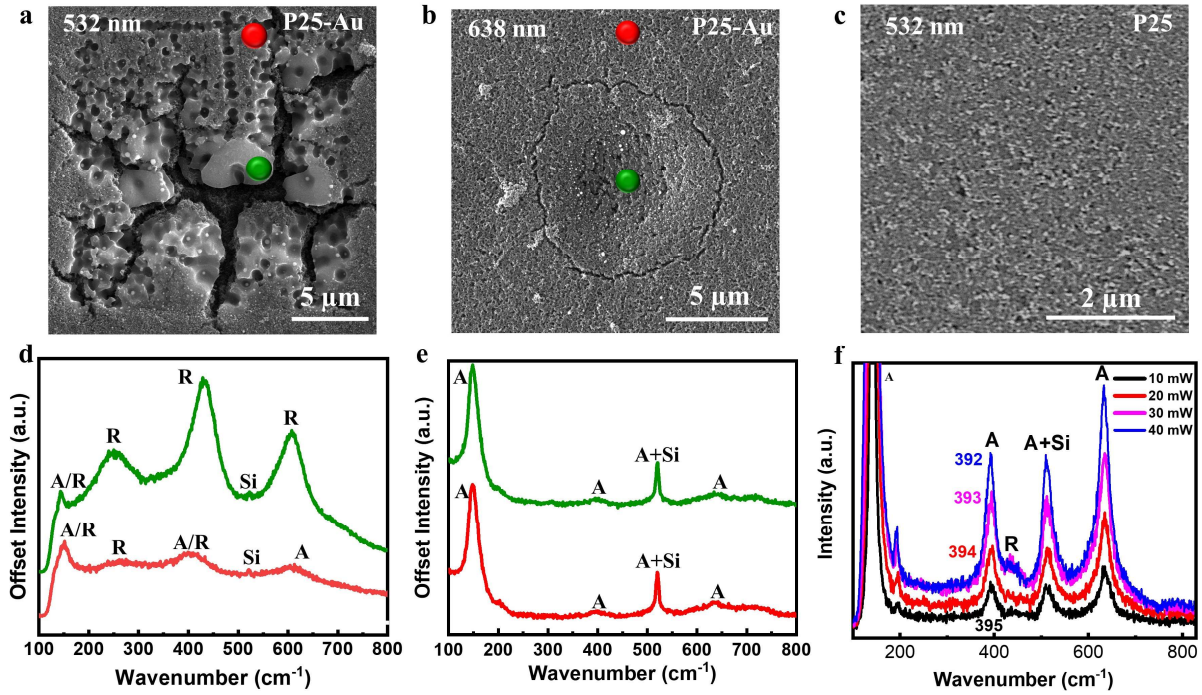

Figure 3: Characterization of P25 film and P25-Au film with on-resonance (532 nm) and off-resonance (638 nm) laser irradiation. SEM images of P25-Au film after laser scanning: **a)** 532 nm at 12 mW and **b)** 638 nm at 18 mW powers. **c)** SEM image of P25 sample after scanned with 532 nm laser at 30mW power. **d)** and **e)** Raman spectra of different spots marked as red dots and green dots in panels a) and b)**,** respectively. **f)** Raman spectra of the P25 taken with a 532 nm laser at various powers during scanning. The anatase peak position at 395 cm^{-1} blue-shifted as the laser power increased due to a temperature change.

In order to check whether the structural change of TiO_2 was because of the presence of LSPR, two different laser wavelengths that were on- and off-resonance with the LSPR of the Au-nanoparticle were used to irradiate the same P25-Au sample. When an on-resonance 532 nm laser

scanned the P25-Au film, the surface morphology was changed, as shown above. Cracks and clumps of melted TiO_2 particles were seen in the SEM image **(Figure 3a)** after irradiated at 12 mW laser power. In comparison, when an off-resonance 638 nm laser at 18 mW power **(Figure 3b)** was used, the surface only had a small crack in the scan area due to the laser heat. The drastic differences of the on- and off-resonance laser irradiation were also observed in an optical microscope image **(Figure S6a).** The effects can be more clearly understood after studying the Raman spectra, which were simultaneously obtained during the scans. At the center area (green spot) with a 532 nm scan, the cluster area had converted to a rutile phase (green curve in **Figure 3d**) due to intense plasmonic heat generated by the Au NPs. At the edge area (red spot), the P25 was only partially converted to rutile as both anatase/rutile were observed, and rutile peak intensity was weaker when compared with the center spot (red curve in **Figure 3d**). For the off-resonance scan, the P25 Raman spectra showed no change. Both the center (green curve) and the edge (red curve) were comparable to the reference P25 spectrum (black curve **Figure 1d**), which was dominated by the anatase phase. Thus, confirming the critical role of LSPR resonance in the heating of the sample.

The laser itself can generate an intense amount of heat on the sample.[53, 68] Here, the role and the effect of laser heating alone were studied by measuring the power-dependence Raman spectra of the P25 thin film without Au NPs. No deformation or cracks were observed on the surface **(Figure 3c and Figure S6b)** when a 532 nm laser at 30 mW irradiated a thin film of P25 sample. Raman spectra **(Figure 3f)** obtained at different laser powers from 10 mW to 40 mW show that the phase of the P25 remains mainly unchanged. Only a tiny peak at 445 cm^{-1} showed the contribution of the rutile phase. The anatase of the B_{1g} mode position shifted from 395 cm^{-1} to 392 cm^{-1} due to a temperature increase caused by laser irradiation, which is far lower than the ART

required temperature of 600 − 700 ºC for P25. Our results showed that plasmonic NPs, Au in this case, and an on-resonance wavelength irradiation attributed to the observed phase transition and melting of the P25 NPs.

This section presents a detailed study of the impact of plasmonic heating on the morphological change in TiO_2 and Au NPs, as observed from SEM, TEM, and EDS images. At 8 mW power, fractures and cracks began to form, as seen from a lower magnification SEM image (**Figure 4.1a**). At the crack's edge (**Figure 4.1b**), a smooth layer of TiO_2 can be observed along with Au particles embedded in the TiO_2 matrix. EDS image (**Figure 4.1d)** of Au and Ti of that area verified that the NPs embedded are indeed Au particles. Those Au NPs are much larger (~100 − 200 nm) than the particles in the area without the crack. Further investigation into the area without cracks at higher magnification and resolution (red cross in Figure 4.1b) revealed two variations of sizes of the Au nanoparticle in **Figure 4.1c**. The larger particles of ~ 50-100 nm were formed from the sintering of the original 25 nm Au NPs, and the smaller particles were less than 10 nm in size. The smaller particles indicate surface evaporation of the original Au NPs at the boiling point. The evaporation of the bulk gold occurs at ~2830°C.[20]

Melting of TiO_2 NPs was observed as the laser power increased. At 16 mW power, aggregations and small pools of melted TiO_2 were seen (**Figure 4.1e**). Investigating further by looking at the melt pools on the left side of the scan area (white box in **Figure 4.1e**), each melt pool had an Au nanoparticle in the middle with size varying from 50-100 nm (**Figures 4.1f-h)**. The size of the melted pools was close to the laser beam size (0.7 μm), so the on-resonance wavelength Gaussian laser beam melted the TiO_2 and formed sintered Au NPs at the center of the melted TiO_2 pools. The melt pool temperature was at least as high as the melting temperature of the TiO_2 NPs, which is known to be around 1830°C.[69-72] Another phenomenon is the balling effect

during laser melting. A molten ball of TiO_2 **(Figure 4i)** was observed after 30 mW laser power irradiation. When the adhesion between the TiO_2 and the silicon substrate weakens, the melted TiO_2 forms a ball instead of adhering to the surface to minimize the surface energy. This is known as the balling effect, commonly observed in the laser powder-bed fusion additive manufacturing.[73, 74] At different laser powers, sintered Au NPs were also seen to be embedded in the TiO_2 matrix **(Figure S7)**. The ball-shaped TiO_2, melted pools of TiO_2, and evaporation of Au indicate that the temperature due to plasmonic heating reached at least as high as 1830°C.

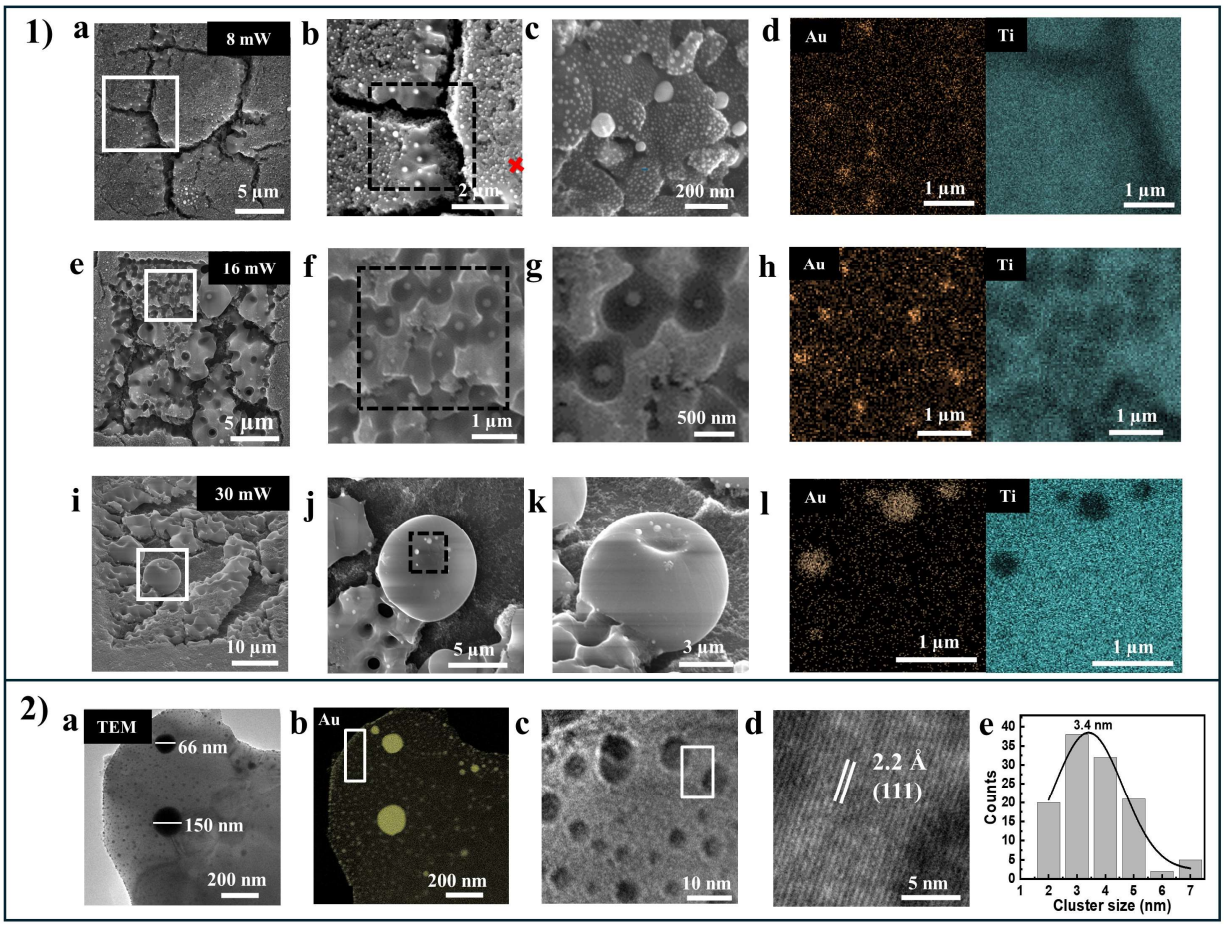

Figure 4.1. Detailed characterization of the P25-Au film after on-resonance laser scanning. SEM image of the irradiated area with 532 nm laser at powers **a)** 8 mW, **e)** 16 mW, and **i)** 30 mW. Zoomed-in SEM image of the white square showing various effects of plasmonic heating seen at

different laser powers: **b)** surface cracks at 8 mW power, **f)** melted pools of TiO_2 at 16 mW power, and **j)** melted TiO_2 ball at 30 mW. **d)**, **h)**, and **l)** The EDS image of Au and Ti elements from the black box square in panels (b), (f), and (j)**,** respectively. High-magnification images showing **c)** evaporated and sintered Au NPs from the red cross marked area in (b); g) melted TiO_2 pools with an Au nanoparticle at the center of pools from the panel (f); **k)** side view of the melted ball-shaped TiO_2 in panel (j). **4.2 a)** TEM image of P25-Au mixture after irradiation with 16 mW laser power, where the darker spots are Au NPs. **b)** Au elemental map from STEM of (a). **c)** The zoomed-in area marked with the white square in panel (b) showing the size and the distribution of evaporated Au NPs. **d)** The high-resolution TEM image of the white square marked area in panel (c) showing the laser-induced rutile phase. **e)** Size distribution chart of evaporated Au NPs from TEM image.

Further morphological changes in Au and P25 NPs were analyzed using a scanning TEM. Another P25-Au film sample was irradiated with 16 mW laser power for TEM imaging. The Au-P25 mixture from a large scan area was separated from the silicon substrate and then transferred to the TEM grid for transmission imaging. A TEM image **(Figure 4.2a)** and the corresponding Au elemental image **(Figure 4.2b)** showed a small area with the sintered and the evaporated Au NPs embedded in TiO_2 with the size of the big, sintered Au particles being 150 nm and 66 nm (HAAD image and EDX map of Ti and O in **Figure S8**). A zoomed-in high-resolution TEM image (**Figure 4.2c**) showed the size of small Au NPs being less than 10 nm. The mean cluster size of the evaporated Au nanoparticle was about 3.4 ± 0.5 nm, as shown in the size distribution chart (**Figure 4.2e**). The evaporated Au NPs were distributed throughout the rutile TiO_2 matrix. The mean size of these smaller particles is about eight times smaller than the original nanoparticle size, confirming the evaporation of the Au. The surrounding TiO_2 matrix was transformed to a rutile phase due to plasmonic heating; a fringe spacing of 2.2 Å can be observed (**Figure 4.2d**),

corresponding to the rutile (111) plane. For comparison, P25 and Au NPs in P25-Au film annealed in an oven at 900 °C showed typical sintering and phase transition phenomena[64-67]. The size of gold NPs increased to 30 − 50 nm, and TiO_2 NPs increased to a few hundred nanometers through the aggregation of adjacent NPs (**Figures S4b** and **S4c**).

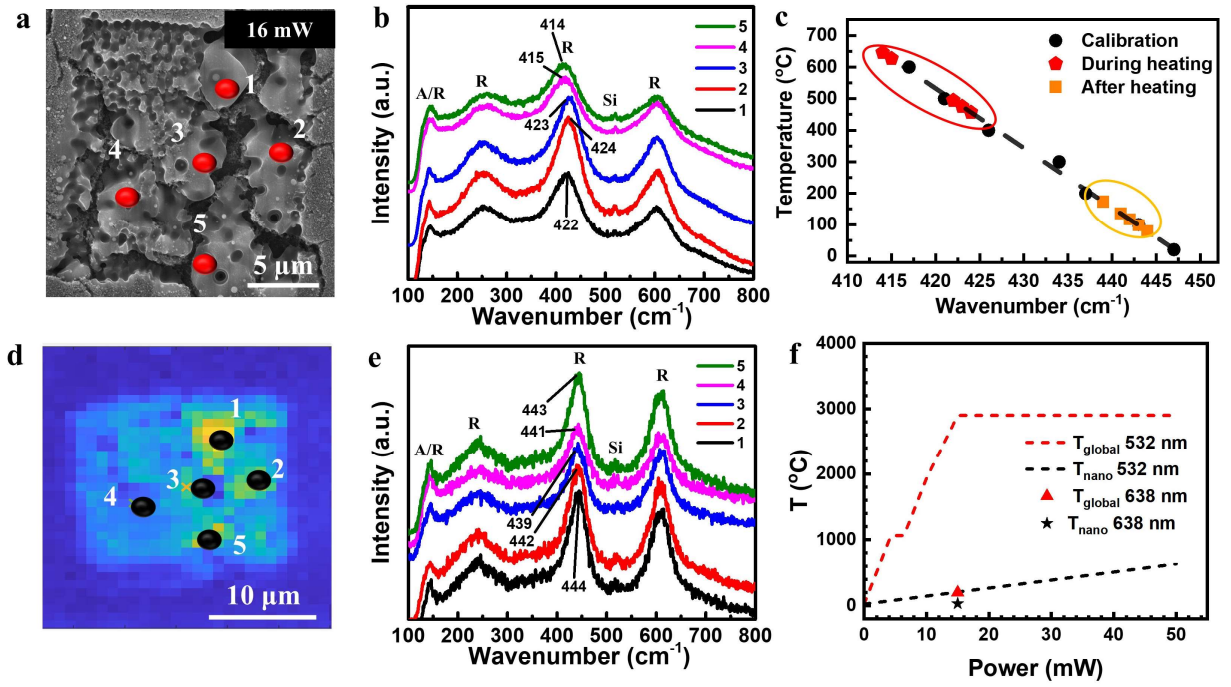

Figure 5: Investigation of temperature changes due to plasmonic heating. **a)** SEM image of the plasmonic heated area with 16 mW laser irradiation. **b)** Raman spectra of 5 different spots (red) highlighted in (a) during plasmonic heating. **c)** A temperature of the plasmonic heated area during heating (red) and after heating (orange) obtained from a calibration curve (black) of the temperature vs wavelength shifts of rutile E_g peak. **d)** Raman map of the plasmonic heated area (16-mW) and surrounding obtained with non-destructive 2 mW laser power after plasmonic heating. **e)** Raman spectra from the same five spots (black in panel (d)) as in (a) after heating. **f)** The dependence of the temperature of Au nanoparticle on the power of 532 nm laser and 638 nm

calculated based on isolated single particle self-heating (black, T_{nano}) and collective/global heating (red, T_{global}).

The temperature dependence of the shift of the Raman peak has been commonly used to measure the temperature.[75-78] Surprisingly, the temperature measured using Raman spectrometry during plasmonic heating is much lower than the expected temperature from the evaporation of the Au NPs and melting of the TiO_2 NPs. Here, a shift in the ~ 446 cm^{-1} Raman peak was used to measure the change in temperature during and after irradiation of the P25-Au mixture. E_g mode (~ 446 cm^{-1}) in the rutile phase has a significant frequency shift as the temperature changes.[76, 78] The 20 x 20 μm^2 Raman map was simultaneously collected when an on-resonance 532 nm laser at 16 mW power (**Figure 5a**) irradiated the P25-Au sample. The laser exposure time at each pixel during the scan was on a 500-millisecond time scale. Raman spectra (**Figure 5b**) from five different spots (marked in red) obtained during the scan show variation of peak shifts of the E_g mode at 422, 424, 423, 415, and 414 cm^{-1}. After completing the 16 mW Raman map scan, the same scan area was rescanned (**Figure 5d**) with 2 mW laser power to check the E_g peak shift after heating. A 2 mW low power was chosen as no morphological changes were observed, so there would be little change in peak shift due to plasmonic heating. The Raman spectra for the same spots (marked in black in Figure 5d) show rutile E_g mode peak shifts at 444, 442, 439, 442, and 443 cm^{-1}. To correspond the E_g peak shifts to temperature changes, a temperature versus Raman shift plot (**Figure 5c**) was calibrated (black dot) by annealing a bulk rutile crystal in a Linkam cell (**Figure S9**). This calibration curve matches the calibration reported by Lan *et al.*[76] During plasmonic heating with 16 mW laser (red marker), the temperature was recorded between 450°C and 650°C, whereas after it had been cooled down, the temperature (blue marker) ranged from 50°C to 150°C. A mean 450°C temperature difference is seen during and after the scan. The

temperature was also calibrated using the stokes and anti-stokes Raman, as seen in **Figure S10**. The obtained temperature range during laser scanning is comparable to the temperature obtained from the Raman peak shift.

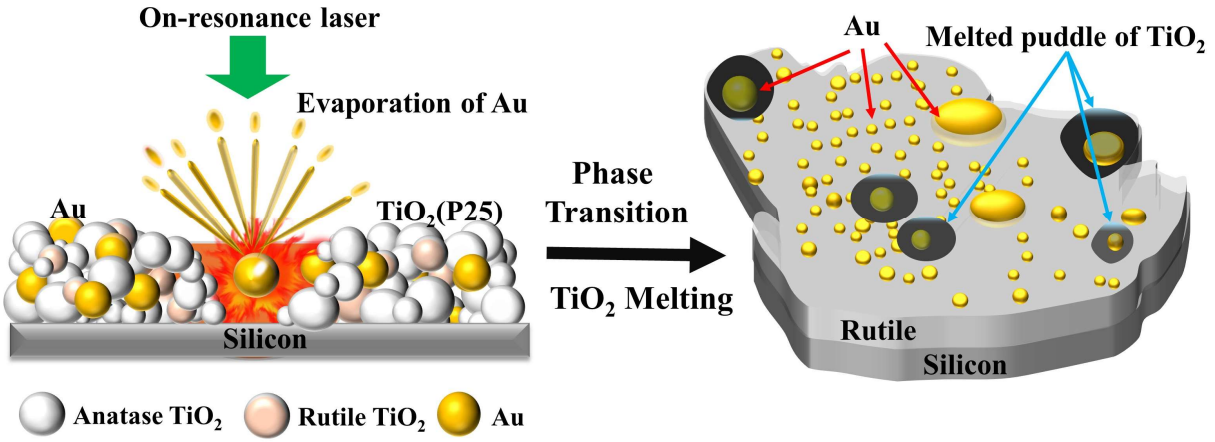

Figure 6: Mechanism of plasmonic heating induced phase transition and melting of the TiO_2 on P25-Au film. **a)** Plasmonic Au NPs absorb light energy, and heat from Au NPs is dispatched to the surrounding TiO_2 medium. Melting, sintering, and vaporization of Au NPs occurred simultaneously; **b)** Au cluster and Au NPs embedded in rutile phase TiO_2 after cooling.

Discussions:

To understand the plasmonic heating mechanism and the discrepancy of the temperature obtained from the Raman thermometry and the melting of the TiO_2, the temperature was calculated using plasmonic heating models.[15, 24, 25, 79] It has been established that when illuminating an ensemble of plasmonic NPs, the heating was not necessarily localized around each nanoparticle. The temperature increase experienced at the center of the illuminated areas results from two contributions. One is self-heating. The other is photothermal collective heating due to heat diffusion or temperature field overlap with other NPs surrounding the NP.[15, 25] Collective heating or global heating could raise the temperature (ΔT_{global}) of the macroscopic region orders of

magnitude higher than that due to self-heating (ΔT_{nano}) even under CW irradiation with moderate laser intensities. The collective heating is related to the number of particles and their inter-distances in the illuminated area. The ratio of these two contributions can be estimated using the dimensionless number $\zeta = \Delta T_{nano}/\Delta T_{global} \sim \frac{p}{3R\sqrt{N}} = \frac{p^2}{3RL} = (3ARL)^{-1}$, where p is the average particle distance, R is the nanoparticle radius, N is the number of NPs under illumination, $L^2 = p^2N$ is the laser irradiated area and A is the nanoparticle area density.[4] In this work, we can estimate ζ to be ~0.05 (with R = 15 nm, A = 600 NPs/μm^2, and L = 700 nm). Such a small ratio indicates that collective heating dominates.

The temperature of a single particle supported on TiO_2 and the global temperature at the center of the laser beam can be calculated.[15, 24, 25] Under CW laser irradiation, the increase of steady-state temperature of a single spherical nanoparticle of radius R depends on the nanoparticle's absorption cross section (σ_{abs}), the light intensity I, and the average thermal conductivity $\bar{\kappa}$ according to

$$\Delta T_{nano} = \frac{\sigma_{abs} I}{4\pi \bar{\kappa} R} \quad (1)$$

The laser beam diameter is obtained assuming a Gaussian beam profile and using experimental optical parameters (NA = 0.50). The laser peak-power density I can be expressed as[20]

$$I = \frac{P(2.3546)^2}{2\pi(FWHM)^2}$$

The σ_{abs} of shining laser on a 30 nm diameter Au nanoparticle decorated on a TiO_2 powder film can be estimated using Mie theory with a refractive index (RI) of ~2.60 and 1.0003 for TiO_2 and air, respectively.[80] The value of σ_{abs} (~1280 nm^2) for the 532 nm laser is much higher than that (60 nm^2) for the 638 nm laser as the resonance of the Au NPs is at 533 nm. The value of thermal

conductivity ($\bar{\kappa}$) is taken as $\bar{\kappa} \approx \frac{\kappa_{TiO} + \kappa_{air}}{2} = \frac{3+0.03}{2} W/mK = 1.5\, W/mK$. The experimental value of the $\bar{\kappa}$ of a dense polycrystalline TiO_2 nanoparticle film is used for that of P25 film.[81, 82] The temperature of a single Au particle (T_{nano}) is shown in **Figure 5f**. The temperature increase was 180 K for 532 nm and 9 K for 638 nm laser irradiation with 15 mW power and 0.7 μm beam size (~ 2.7 x 10^6 W/cm^2 or 27 mW/μm^2). The temperature increase from the resonance (532 nm) irradiation is about 20 times that from the non-resonance (638 nm) irradiation. However, this rise in temperature from a single Au nanoparticle could not account for the observed Au surface evaporation and melting of the TiO_2 NPs, even under resonance irradiation. This estimated temperature increase is consistent with the estimation by Baffou *et al.*[24] In another study using similar CW laser irradiance, Setoura *et al.* observed the surface evaporation of Au NPs into satellite NPs when well-dispersed (>10 μm apart) single Au NPs with a 100 nm diameter were irradiated on glass.[20] The estimated single particle temperature is about an order of magnitude higher than the single particle temperature estimated in our study. This is because the thermal conductivity of glass is much less than that of TiO_2. The effective $\bar{\kappa}$ (0.2 W/mK) for the air/glass is about five times smaller than the air/TiO_2 interface. Additionally, the larger particle (100 nm in diameter) has an order of magnitude larger cross-section than the 30 nm Au particles. The collective heating effect was not considered in Setoura *et al.*'s work because of the significant separation (10 μm) between the particles.

The temperature increase due to the collective heating (ΔT_{global}) can be estimated according to $\Delta T_{global} = \frac{\sigma_{abs} P}{\pi \kappa D a}\left(1 - \frac{2\sqrt{a}}{\sqrt{\pi} D}\right)$, where a is the average unit area of particle lattice, and D is the beam diameter.[15] As shown in **Figure 5f**, when the power is greater than 15 mW (*i.e.*, 27 mW/μm^2), the global temperature of the Au nanoparticle reaches the bulk boiling temperature, ~ 2800 ºC. The melting enthalpy (1.22 ×10^9 J m^{-3}) at 1044 ºC was added to the estimation. This temperature

increase is an order of magnitude higher than the increase due to the self-heating at the plasmonic resonance. The collective temperature increase is about 1 K per 0.007 mW/μm^2.

At such a high particle temperature, it is unsurprising that we observed the formation of small (~ 3 nm) Au particles, which were expected from the surface evaporation of the plasmonic Au NPs. This observation was similar to the surface evaporation of the Au NPs at the air/glass interface observed by Setoura *et al.*[20] Orders of magnitude higher temperatures than the estimated self-heating temperature were observed in the case of water boiling when solar light illuminated a solution of highly concentrated gold NPs.[21] Bauton *et al.* suggested that collective thermal effects must be considered to account for the contradiction between the experimental observation of water boiling and the small temperatures estimated using self-heating.[24]

Figure 6 shows the proposed melting process of the TiO_2 due to plasmonic heating. When Au plasmonic NPs supported on TiO_2 porous nanoparticle thin film were irradiated by CW-laser at the plasmonic wavelength, the temperature of the Au NPs increased as a result of both the localized self-heating and the collective heating. Under the steady-state heating by a CW laser, the time evolution of the single particle to reach the equilibrium temperature (~ 210 ºC) has been estimated to be an order of 0.07 ns ($\tau_{nano} = {r_p}^2$/D ~ 0.07 ns, using thermal diffusivity of TiO_2 $D = 3 \times 10^{-6}\, m^2/s$ and r_p = 15 nm).[20, 25] The time scale for thermal fields to overlap between neighboring particles with a particle density of 600 particles/μm^2 can be estimated as $\tau_0 = {d_{pp}}^2$/D ~ 0.5 ns which is about seven times the time scale for a single particle to reach to equilibrium temperature. The time scale for heat diffusion across the laser beam (0.7×0.7 μm^2) is $\tau_{global} = L^2$/D ~ 0.16 μs. This indicates that the laser-irradiated area reached a temperature close to the bulk boiling point (~2800 ºC) of Au in about 0.16 μs, much faster than the integration time (500 ms) used to take Raman spectra. After the temperature reached the boiling temperature of the Au, the

heat dissipation and the structural evolution process of the Au-TiO_2 matrix became complex. The Au particle evaporated at the surface and splattered gold droplets with a size of ~3 nm to the surrounding area. The heat dissipation melted the TiO_2 NPs in the laser beam, forming a liquid TiO_2 phase mixed with Au NPs. The melting of TiO_2 would cool down the temperature of the mixer. The evaporation of Au reduced the particle size of individual Au particles. This lowered the absorption cross-section, therefore slowing down the heating rate. The Au NPs with a reduced size diffused and sintered to bigger spherical Au particles (e.g., ~100 nm at 16 mW). As Au is heavier than TiO_2, large Au particles sunk into the liquid pool of TiO_2. The sintering would further change the absorption cross-section for the self-heating and reduce the number of particles contributing to the collective heating. Therefore, the temperature estimation after the boiling temperature is more complicated and needs appropriate numerical simulations.

The collective heating due to plasmonic absorption impacts various applications, including plasmon photochemistry, which has become a hot topic, and powder-bed additive manufacturing (AM), which has yet to be explored. The relative thermal and non-thermal contribution (e.g., hot carriers) in the plasmon-drive process has been under extensive debate regarding the application of photocatalysis.[24, 31-34] The distinguishment requires accurately measuring the actual temperature of the plasmonic particle and the surrounding matrix (e.g., TiO_2). *Via* shape-changing and surface evaporation, it is known that the temperature of the Au NPs and other plasmonic particles can reach melting temperature and boiling temperature under moderate laser irradiance. Theory simulations predicted these high temperatures.[19] However, the impact of the plasmonic heating on the surrounding catalysts and the photocatalytic reaction is still unclear. Different approaches have been developed to measure the temperature accurately. Most of the developed techniques are based on optical measurements, including Raman spectroscopy,[75-78] fluorescence anti-stokes emission of

metal NPs[83], and quadriwave shearing interferometry.[15, 84] The time needed to take a spectrum is about 10-100 ms, which is longer than the τ_{global} (~ 0.2 μs) for a focused CW laser beam and the τ_{global} (~ 130 μs) for an unfocused CW laser beam (e.g. 20 μm diameter in air). The temperature measured from the optical spectroscopy is a time average of the temperature from the rising of the temperature to partially cooled down. Therefore, the temperature measured from the optical measurements would not catch the maximum temperature that the Au and TiO_2 reached. To check this hypothesis, spectra were taken every 25 ms from when the laser was on. The E_g mode shifts (**Figure S11a**) from 387 cm^{-1} at 75 ms to 410 cm^{-1} at 4150 ms, representing the decay of the temperature from about 1150 ºC to 715 ºC (**Figure S11b**). Note that 25 ms is the smallest time interval for our spectrometer. A pump and probe experiment should be able to catch the transient temperature. Our results show that most optical methods measure the time-averaged temperature and miss the transient temperature (T_{global}) due to the collective photothermal heating even under CW laser irradiation. Similar temperature inconsistency has been encountered in laser-based additive manufacturing.[85, 86] Recently, a high-speed (100 kHz) coaxial camera imaging setup has been developed to resolve the time and spatial evolution of the laser melting and melt pool cooling.[68] The time scale of the metal powder reaching maximum temperature was about 50 μs, much less than the integration time in the Raman spectrometry.

The result of this study highlights the profound effect of collective heating on the possible parameter space for CW photothermal catalysis. Under CW laser irradiation, collective heating enabled high temperatures (e.g., melting temperature of TiO_2) to be reached under moderate laser power. The temperature of the plasmonic Au nanoparticle rose to the maximum temperature in a short time (~ 0.16 μs). Within this brief period, the surrounding TiO_2 experienced the same high temperature as the Au NPs due to collective heating. Our work shows experimental evidence that

photothermal heating from CW illumination could introduce phase transition of the catalyst and reach as high as a couple of thousand Kevin in photoreaction. The results suggest that the photothermal effect could be a significant mechanism in the plasmon-assisted photocatalytic reactions.

For AM applications, a high-power (40-80 mW/um^2) laser has been used to melt stainless steel powder for 3D metal printing. A new approach to take advantage of plasmonic heating, for example, adding 1% of plasmonic particles to the stainless-steel powder, could significantly reduce the laser power needed. An estimation from the collective heating, as presented above, indicates that the boiling temperature of 4000 K can be reached by CW laser with a laser irradiance of less than 20 mW/um^2 from the plasmonic heating of 30 nm Au plasmonic particles. Here, the heating generated from the light absorption of stainless steel is not included in the estimation. Stainless steel is only taken as a substrate for heat dissipation. The reported thermal conductivity (0.2 W/mK) of various popular AM stainless steel powders was used, about 1/10th to 1/100th of the solid bulk thermal conductivities. In other words, the additional collective heating generated by Au plasmonic particles would significantly reduce the laser power needed to melt stainless steel powder. The laser irradiance is the same as used on TiO_2 in this study. In these applications, Au NPs can be replaced by alternative plasmonic materials, e.g., aluminum. Al is economically more sustainable than Au. Its plasmonic wavelength is tunable in a wide wavelength range. The calculation shows that the plasmonic photothermal heating of stainless steel (~3600 K) could be accomplished by Al NPs with a size of 100 nm under the same laser irradiance (22 mW/um^2, or 2×10^{10} W/m^2). A simple economic ultrasonication method has been reported recently to synthesize Al plasmonic NPs from commercial Al foil.[87]

Conclusions:

Morphological and molecular structural effects of plasmonic heating on the Au-decorated P25 TiO_2 NP porous film have been studied. With the increase of the power of a laser whose wavelength is in resonance with the LSPR of Au NPs, the phase of P25 transformed from mainly anatase phase to a rutile phase, accompanied by the formation of cracks and aggregates. At higher laser power, agglomerations of melted TiO_2 were observed, indicating that the matrix surrounding the Au NPs reached a temperature as high as the melting temperature of TiO_2, 1830 ºC. The irradiation at the off-resonance laser wavelength did not result in phase transition and the melting of TiO_2, which confirms the role of plasmonic heating. The calculation shows that collective heating dominates the contribution to the melting of TiO_2. However, the temperature measured using Raman spectroscopy was much lower than the transient temperature that Au and TiO_2 NPs experienced. The results suggested that optical measurement often misses the high transient temperature that the Au and TiO_2 experienced in the photocatalytic reactions. The experiment observation of the high temperature of the supporting matrix (e.g., thousands of Kelvins) suggests the potential new application of plasmonic heating, such as additive manufacturing.

Methods:

Materials and Sample Preparation

P25 TiO_2 (purity: >99.5%) was purchased from Sigma-Aldrich (Sigma-Aldrich, St. Louis, MO). Au NPs were synthesized using chemical reduction of the 0.25 mM gold precursor $HAuCl_4$ by 0.25 mM trisodium citrate at 100 ºC for 20 min.[88] In preparation for the P25 film, 1.5 grams of P25 powder were mixed and ground well with 3 ml ethylene glycol to form a smooth paste. Then, it was spread onto a Si or glass substrate with a blade in the space between transparent

tape.[89] The thickness of the tape determined the thickness of the P25 film. Then, the P25 films were dried overnight at 200 ºC in the air for 2 hours and designated as-prepared P25 films. The as-prepared P25 was immersed into the gold nanoparticle aqueous solution overnight to obtain the Au-decorated P25 film, which was washed with water to remove loosely attached Au NPs and then dried overnight at 75 ºC.

Characterization and Instrumentation

Laser irradiation and scanning were carried out by a lab-built confocal Raman system, which consists of a 532 nm continuous laser source with a maximum power of 55 mW and a Zaber ASR-E closed-loop microscope stage (Zaber Technologies Inc., Canada) for scanning and focusing control.[61] An Olympus (MPLFLN50X) objective lens (50×, NA = 0.50) with ~0.7 μm beam spot size was used to scan over the samples' surface, and the optical shutter of the spectrometer controlled the exposure time. Assuming the Gaussian beam profile, the calculated $1/e^2$ diameter of the focused laser beam was 0.61 μm using the optical parameters in the setup (λ =532 nm, M^2 =1, focal length of the objective = 3.6 mm, beam diameter at lens =4 mm). However, experimentally, the beam profile was a tad asymmetrical, and the beam spot size of ~ 0.7 μm was measured from the SEM image of the individual melted TiO_2 matrix due to plasmonic heating. The movement of the stages was controlled by MATLAB codes programmed in our lab. In a typical plasmonic heating scanning, the scanning area was 20 μm x 20 μm with a 40-pixel × 40-pixel resolution. The laser expose time at each pixel is 500 milliseconds. The laser power was adjusted with an NDC-100C-4M filter (Thorlabs, Newton, NJ, USA). The Raman spectra were collected using a Princeton Instruments SCT-320 spectrometer with an 1800 lines/mm grating at the same time as the laser-induced plasmonic heating. The peak of Si at 520.4 cm^{-1} was used as the calibration for all the Raman spectral analyses.

The X-ray diffraction patterns of the TiO_2 and TiO_2 -Au were collected with a Siemens D5000 diffractometer (Munich, Germany) in θ-2θ mode using Cu Kα radiation (λ = 1.5406 Å) as the X-ray source (operated at 40 kV and 30 A). The scanning step size for XRD was 0.05°. Scanning electron micrographs were collected with a Focused Ion Beam Scanning Electron Microscope (SEM; Versa 3D, Thermo Fisher, formerly FEI, Hillsboro, OR, USA) at 30 kV. Energy-dispersive X-ray spectroscopy (EDS) experiments were performed with an Octan Pro EDS detector (Ametek, Berwyn, PA, USA) to determine the element composition of TiO_2 patterns at 20 kV with spot size 7. High-resolution transmission electron micrographs of the samples were obtained using a Transmission Electron Microscope (TEM, Thermo Fisher Spectra 300C) with TEM and Scanning-TEM (STEM) imaging modes operated at 300 kV.

Acknowledgement:

This work was supported by the National Science Foundation under Grant CHE-2247107. The authors acknowledge the support of the Center for Microscopy and Imaging at Baylor University. The authors express their gratitude to Steve Dworkin from the Department of Geosciences at Baylor University for generously granting permission to utilize the XRD equipment for this study. The authors would like to thank Lucy Lu for the image analysis.

Supporting Information Available: Additional information in Figures S1-S8 display optical image, SEM images, TEM images, Raman spectra, and Figure S9-S10 shows temperature calibration results, and Figure S11 displays the time dependence temperature shift measurements

References

(1) Yang, B.; Li, C. Y.; Wang, Z. F.; Dai, Q. Thermoplasmonics in Solar Energy Conversion: Materials, Nanostructured Designs, and Applications. *Adv Mater* **2022**, *34* (26). DOI: 10.1002/adma.202107351.

(2) Zhang, J. Q.; Chen, H. J.; Duan, X. G.; Sun, H. Q.; Wang, S. B. Photothermal catalysis: From fundamentals to practical applications. *Mater Today* **2023**, *68*, 234-253. DOI: 10.1016/j.mattod.2023.06.017.

(3) Kang, L. L.; Liu, X. Y.; Wang, A. Q.; Li, L.; Ren, Y. J.; Li, X. Y.; Pan, X. L.; Li, Y. Y.; Zong, X.; Liu, H.; et al. Photo-thermo Catalytic Oxidation over a TiO_2-WO_3-Supported Platinum Catalyst. *Angew Chem Int Edit* **2020**, *59* (31), 12909-12916. DOI: 10.1002/anie.202001701.

(4) Jain, P. K. Taking the Heat Off of Plasmonic Chemistry. *J Phys Chem C* **2019**, *123* (40), 24347-24351. DOI: 10.1021/acs.jpcc.9b08143.

(5) Zhao, F.; Guo, Y. H.; Zhou, X. Y.; Shi, W.; Yu, G. H. Materials for solar-powered water evaporation. *Nat Rev Mater* **2020**, *5* (5), 388-401. DOI: 10.1038/s41578-020-0182-4.

(6) Gao, M. M.; Zhu, L. L.; Peh, C. K.; Ho, G. W. Solar absorber material and system designs for photothermal water vaporization towards clean water and energy production. *Energ Environ Sci* **2019**, *12* (3), 841-864. DOI: 10.1039/c8ee01146j.

(7) Huang, X.; Jain, P. K.; El-Sayed, I. H.; El-Sayed, M. A. Plasmonic photothermal therapy (PPTT) using gold nanoparticles. *Lasers Med Sci* **2008**, *23* (3), 217-228. DOI: 10.1007/s10103-007-0470-x From NLM Medline.

(8) Kim, M.; Lee, J. H.; Nam, J. M. Plasmonic Photothermal Nanoparticles for Biomedical Applications. *Adv Sci (Weinh)* **2019**, *6* (17), 1900471. DOI: 10.1002/advs.201900471 From NLM.

(9) Xu, C.; Pu, K. Y. Second near-infrared photothermal materials for combinational nanotheranostics. *Chem Soc Rev* **2021**, *50* (2), 1111-1137. DOI: 10.1039/d0cs00664e.

(10) Roberts, A. T.; Yang, J.; Reish, M. E.; Alabastri, A.; Halas, N. J.; Nordlander, P.; Everitt, H. O. Plasmonic nanoparticle-based epoxy photocuring: A deeper look. *Materials today.* **2019**, *27*, 14-20. DOI: 10.1016/j.mattod.2018.09.005.

(11) Jauffred, L.; Samadi, A.; Klingberg, H.; Bendix, P. M.; Oddershede, L. B. Plasmonic Heating of Nanostructures. *Chem Rev* **May 24, 2019**. DOI: 10.1021/acs.chemrev.8b00738.

(12) Brongersma, M. L.; Halas, N. J.; Nordlander, P.; Brongersma, M. L.; Halas, N. J.; Nordlander, P. Plasmon-induced hot carrier science and technology. *Nature Nanotechnology 2015 10:1* **2015-01-06**, *10* (1). DOI: 10.1038/nnano.2014.311.

(13) Cui, X. M.; Ruan, Q. F.; Zhu, X. L.; Xia, X. Y.; Hu, J. T.; Fu, R. F.; Li, Y.; Wang, J. F.; Xu, H. X. Photothermal Nanomaterials: A Powerful Light-to-Heat Converter. *Chem Rev* **2023**, *123* (11), 6891-6952. DOI: 10.1021/acs.chemrev.3c00159.

(14) Bora, T.; Zoepfl, D.; Dutta, J. Importance of Plasmonic Heating on Visible Light Driven Photocatalysis of Gold Nanoparticle Decorated Zinc Oxide Nanorods. *Sci Rep-Uk* **2016**, *6*. DOI: 10.1038/srep26913.

(15) Baffou, G.; Berto, P.; Ureña, E. B.; Quidant, R.; Monneret, S.; Polleux, J.; Rigneault, H. Photoinduced Heating of Nanoparticle Arrays. *Acs Nano* **2013**, *7* (8), 6478-6488. DOI: 10.1021/nn401924n.

(16) Alessandri, I.; Depero, L. E. Using plasmonic heating of gold nanoparticles to generate local SER(R)S-active TiO_2 spots. *Chem Commun* **2009**, (17), 2359-2361. DOI: 10.1039/b900647h.

(17) Xu, Y. R.; Zhao, X. G.; Li, A. B.; Yue, Y. N.; Jiang, J.; Zhang, X. Plasmonic heating induced by Au nanoparticles for quasi-ballistic thermal transport in multi-walled carbon nanotubes. *Nanoscale* **2019**, *11* (16), 7572-7581. DOI: 10.1039/c9nr00901a.

(18) Richardson, H. H.; Carlson, M. T.; Tandler, P. J.; Hernandez, P.; Govorov, A. O. Experimental and Theoretical Studies of Light-to-Heat Conversion and Collective Heating Effects in Metal Nanoparticle Solutions. *Nano Lett* **2009**, *9* (3), 1139-1146. DOI: 10.1021/nl8036905.
(19) Setoura, K.; Ito, S. Quantifying the durability of transition metal nitrides in thermoplasmonics at the single-nanoparticle level. *AIP Advances* **2021/11/01**, *11* (11). DOI: 10.1063/5.0074139.
(20) Kenji Setoura; Yudai Okada; Shuichi Hashimoto; Kenji Setoura; Yudai Okada; Shuichi Hashimoto. CW-laser-induced morphological changes of a single gold nanoparticle on glass: observation of surface evaporation. *Physical Chemistry Chemical Physics* **2014/11/19**, *16* (48). DOI: 10.1039/C4CP03733B.
(21) Neumann, O.; Urban, A. S.; Day, J.; Lal, S.; Nordlander, P.; Halas, N. J. Solar Vapor Generation Enabled by Nanoparticles. **November 28, 2012**. DOI: 10.1021/nn304948h.
(22) Zhou, L.; Swearer, D. F.; Zhang, C.; Robatjazi, H.; Zhao, H.; Henderson, L.; Dong, L.; Christopher, P.; Carter, E. A.; Nordlander, P.; Halas, N. J. Quantifying hot carrier and thermal contributions in plasmonic photocatalysis. *Science* **2018-10-05**, *362* (6410). DOI: 10.1126/science.aat6967.
(23) Mascaretti, L.; Naldoni, A. Hot electron and thermal effects in plasmonic photocatalysis. *Journal of Applied Physics* **2020/07/28**, *128* (4). DOI: 10.1063/5.0013945.
(24) Baffou, G.; Bordacchini, I.; Baldi, A.; Quidant, R.; Baffou, G.; Bordacchini, I.; Baldi, A.; Quidant, R. Simple experimental procedures to distinguish photothermal from hot-carrier processes in plasmonics. *Light: Science & Applications 2020 9:1* **2020-06-28**, *9* (1). DOI: 10.1038/s41377-020-00345-0.
(25) Keblinski, P.; Cahill, D. G.; Bodapati, A.; Sullivan, C. R.; Taton, T. A. Limits of localized heating by electromagnetically excited nanoparticles. *Journal of Applied Physics* **2006/09/01**, *100* (5). DOI: 10.1063/1.2335783.
(26) Setoura, K.; Werner, D.; Hashimoto, S. Optical Scattering Spectral Thermometry and Refractometry of a Single Gold Nanoparticle under CW Laser Excitation. *The Journal of Physical Chemistry C* **July 16, 2012**, *116* (29). DOI: 10.1021/jp304271d.
(27) Ingram, D. B.; Linic, S. Water Splitting on Composite Plasmonic-Metal/Semiconductor Photoelectrodes: Evidence for Selective Plasmon-Induced Formation of Charge Carriers near the Semiconductor Surface. **March 22, 2011**. DOI: 10.1021/ja200086g.
(28) Boerigter, C.; Campana, R.; Morabito, M.; Linic, S.; Boerigter, C.; Campana, R.; Morabito, M.; Linic, S. Evidence and implications of direct charge excitation as the dominant mechanism in plasmon-mediated photocatalysis. *Nature Communications 2015 7:1* **2016-01-28**, *7* (1). DOI: 10.1038/ncomms10545.
(29) Caretti, I.; Keulemans, M.; Verbruggen, S. W.; Lenaerts, S.; Van Doorslaer, S.; Caretti, I.; Keulemans, M.; Verbruggen, S. W.; Lenaerts, S.; Van Doorslaer, S. Light-Induced Processes in Plasmonic Gold/TiO2 Photocatalysts Studied by Electron Paramagnetic Resonance. *Topics in Catalysis 2015 58:12* **2015-08-04**, *58* (12). DOI: 10.1007/s11244-015-0419-4.
(30) Guseinov, N.; Prikhodko, O.; Yergaliyeva, S.; Nemkayeva, R.; Aitzhanov, M.; Arbuz, A.; Orynbay, B.; Mukhametkarimov, Y.; Sagidolda, Y.; Ismailova, G.; et al. Synthesis and optical properties of Ag/Au-TiO_2 plasmonic composite thin films. *Optical Materials Express, Vol. 13, Issue 10, pp. 2726-2736* **2023-10-01**, *13* (10). DOI: 10.1364/OME.495430.
(31) Hamans, R. F.; Parente, M.; Baldi, A. Super-Resolution Mapping of a Chemical Reaction Driven by Plasmonic Near-Fields. *Nano Lett* **February 19, 2021**, *21* (5). DOI: 10.1021/acs.nanolett.0c04837.

(32) Ou, W.; Zhou, B.; Shen, J.; Lo, T. W.; Lei, D.; Li, S.; Zhong, J.; Li, Y. Y.; Lu, J. Thermal and Nonthermal Effects in Plasmon - Mediated Electrochemistry at Nanostructured Ag Electrodes. *Angewandte Chemie* **2020/04/20**, *132* (17). DOI: 10.1002/ange.202001152.
(33) Zhang, Q.; Zhou, Y.; Fu, X.; Villarreal, E.; Sun, L.; Zou, S.; Wang, H. Photothermal Effect, Local Field Dependence, and Charge Carrier Relaying Species in Plasmon-Driven Photocatalysis: A Case Study of Aerobic Nitrothiophenol Coupling Reaction. *The Journal of Physical Chemistry C* **October 4, 2019**, *123* (43). DOI: 10.1021/acs.jpcc.9b08181.
(34) Rodio, M.; Graf, M.; Schulz, F.; Mueller, N. S.; Eich, M.; Lange, H. Experimental Evidence for Nonthermal Contributions to Plasmon-Enhanced Electrochemical Oxidation Reactions. *ACS Catalysis* **January 21, 2020**, *10* (3). DOI: 10.1021/acscatal.9b05401.
(35) Yonatan Sivan; Wai Un, I.; Yonatan Dubi; Yonatan Sivan; Wai Un, I.; Yonatan Dubi. Assistance of metal nanoparticles in photocatalysis – nothing more than a classical heat source. *Faraday Discussions* **2019/05/23**, *214* (0). DOI: 10.1039/C8FD00147B.
(36) Yonatan Dubi; Wai Un, I.; Yonatan Sivan; Yonatan Dubi; Wai Un, I.; Yonatan Sivan. Thermal effects – an alternative mechanism for plasmon-assisted photocatalysis. *Chemical Science* **2020/05/20**, *11* (19). DOI: 10.1039/C9SC06480J.
(37) Dubi, Y.; Sivan, Y.; Dubi, Y.; Sivan, Y. "Hot" electrons in metallic nanostructures—non-thermal carriers or heating? *Light: Science & Applications 2019 8:1* **2019-10-02**, *8* (1). DOI: 10.1038/s41377-019-0199-x.
(38) Gouma, P. I.; Mills, M. J. Anatase-to-rutile transformation in titania powders. *Journal of the American Ceramic Society* **2001**, *84* (3), 619-622. DOI: 10.1111/j.1151-2916.2001.tb00709.x (acccessed Mar).
(39) Czanderna, A. W.; Rao, C. N. R.; Honig, J. M. The anatase-rutile transition. Part 1.—Kinetics of the transformation of pure anatase. *Transactions of the Faraday Society* **1958**, *54* (0), 1069-1073. DOI: 10.1039/TF9585401069.
(40) Hanaor, D. A. H.; Sorrell, C. C. Review of the anatase to rutile phase transformation. *Journal of Materials Science* **2011**, *46* (4), 855-874. DOI: 10.1007/s10853-010-5113-0 (acccessed Feb).
(41) Ma, H. L.; Yang, J. Y.; Dai, Y.; Zhang, Y. B.; Lu, B.; Ma, G. H. Raman study of phase transformation of TiO_2 rutile single crystal irradiated by infrared femtosecond laser. *Appl Surf Sci* **2007**, *253* (18), 7497-7500. DOI: 10.1016/j.apsusc.2007.03.047.
(42) Dauksta, E.; Medvids, A.; Onufrijevs, P.; Shimomura, M.; Fukuda, Y.; Murakami, K. Laser-induced crystalline phase transition from rutile to anatase of niobium doped TiO_2. *Curr Appl Phys* **2019**, *19* (3), 351-355. DOI: 10.1016/j.cap.2018.12.018.
(43) Ricci, P. C.; Casu, A.; Salis, M.; Corpino, R.; Anedda, A. Optically Controlled Phase Variation of TiO_2 Nanoparticles. *J Phys Chem C* **2010**, *114* (34), 14441-14445. DOI: 10.1021/jp105091d.
(44) Ricci, P. C.; Carbonaro, C. M.; Stagi, L.; Salis, M.; Casu, A.; Enzo, S.; Delogu, F. Anatase-to-Rutile Phase Transition in TiO_2 Nanoparticles Irradiated by Visible Light. *J Phys Chem C* **2013**, *117* (15), 7850-7857. DOI: 10.1021/jp312325h.
(45) Alessandri, I.; Ferroni, M.; Depero, L. E. In Situ Plasmon-Heating-induced Generation of Au/TiO_2 "Hot Spots" on Colloidal Crystals. *Chemphyschem* **2009**, *10* (7), 1017-1022. DOI: 10.1002/cphc.200900080.
(46) Sapsford, K. E.; Algar, W. R.; Berti, L.; Gemmill, K. B.; Casey, B. J.; Oh, E.; Stewart, M. H.; Medintz, I. L. Functionalizing Nanoparticles with Biological Molecules: Developing Chemistries that Facilitate Nanotechnology. **February 22, 2013**. DOI: 10.1021/cr300143v.

(47) Wang, G.; Xu, L.; Zhang, J.; Yin, T.; Han, D.; Wang, G.; Xu, L.; Zhang, J.; Yin, T.; Han, D. Enhanced Photocatalytic Activity of Powders (P25) via Calcination Treatment. *International Journal of Photoenergy* **2012/2/19**, *2012*. DOI: 10.1155/2012/265760.
(48) Belekoukia, M.; Kalamaras, E.; Tan, J. Z. Y.; Vilela, F.; Garcia, S.; Maroto-Valer, M. M.; Xuan, J. Continuous flow-based laser-assisted plasmonic heating: A new approach for photothermal energy conversion and utilization. *Applied energy* **2019**, *247*, 517-524. DOI: 10.1016/j.apenergy.2019.04.069.
(49) Jiang, X.; Manawan, M.; Feng, T.; Qian, R.; Zhao, T.; Zhou, G.; Kong, F.; Wang, Q.; Dai, S.; Pan, J. H. Anatase and rutile in evonik aeroxide P25: Heterojunctioned or individual nanoparticles? *Catalysis today* **2018**, *300*, 12-17. DOI: 10.1016/j.cattod.2017.06.010.
(50) Ren, X.; Ren, X.; Song, Y.; Song, Y.; Liu, A.; Liu, A.; Zhang, J.; Zhang, J.; Yang, P.; Yang, P.; et al. Experimental and theoretical studies of DMH as a complexing agent for a cyanide-free gold electroplating electrolyte. *RSC Advances* **2015/07/29**, *5* (80). DOI: 10.1039/C5RA13140E.
(51) Uddin, M. J.; Cesano, F.; Chowdhury, A. R.; Trad, T.; Cravanzola, S.; Martra, G.; Mino, L.; Zecchina, A.; Scarano, D. Surface Structure and Phase Composition of TiO2 P25 Particles After Thermal Treatments and HF Etching. *Frontiers in Materials* **2020/07/07**, *7*. DOI: 10.3389/fmats.2020.00192.
(52) Chu, L.; Qin, Z.; Yang, J.; Li, X. a. Anatase TiO2 Nanoparticles with Exposed {001} Facets for Efficient Dye-Sensitized Solar Cells. *Sci Rep-Uk* **2015**, *5* (1). DOI: 10.1038/srep12143.
(53) Ming, L.; Ming, L.; Yang, H.; Yang, H.; Zhang, W.; Zhang, W.; Zeng, X.; Zeng, X.; Xiong, D.; Xiong, D.; et al. Selective laser sintering of TiO2 nanoparticle film on plastic conductive substrate for highly efficient flexible dye-sensitized solar cell application. *Journal of Materials Chemistry A* **2014/03/04**, *2* (13). DOI: 10.1039/C3TA14210H.
(54) Machín, A.; Soto-Vázquez, L.; Colón-Cruz, C.; Valentín-Cruz, C. A.; Claudio-Serrano, G. J.; Fontánez, K.; Resto, E.; Petrescu, F. I.; Morant, C.; Márquez, F.; et al. Photocatalytic Activity of Silver-Based Biomimetics Composites. *Biomimetics 2021, Vol. 6, Page 4* **2021-01-04**, *6* (1). DOI: 10.3390/biomimetics6010004.
(55) Sirtori, C.; Freitas, A. M. d.; Fujiwara, S. T.; Peralta-Zamora, P. Photocatalytic degradation of camphor by suspended and immobilized photocatalysts. *Journal of the Brazilian Chemical Society* **2012-08**, *23* (8). DOI: 10.1590/S0103-50532012005000020.
(56) Ceballos-Chuc, M. C.; Ramos-Castillo, C. M.; Alvarado-Gil, J. J.; Oskam, G.; Rodríguez-Gattorno, G. Influence of Brookite Impurities on the Raman Spectrum of TiO2 Anatase Nanocrystals. *The Journal of Physical Chemistry C* **August 4, 2018**, *122* (34). DOI: 10.1021/acs.jpcc.8b04987.
(57) Ohsaka, T.; Izumi, F.; Fujiki, Y. Raman spectrum of anatase, TiO2. *Journal of Raman Spectroscopy* **1978/12/01**, *7* (6). DOI: 10.1002/jrs.1250070606.
(58) Zeng, G.; Li, K.-K.; Yang, H.-G.; Zhang, Y.-H. Micro-Raman mapping on an anatase TiO2 single crystal with a large percentage of reactive (001) facets. *Vibrational spectroscopy* **2013**, *68*, 279-284. DOI: 10.1016/j.vibspec.2013.08.012.
(59) Chang, H.; Huang, P. J. Thermo-Raman studies on anatase and rutile. *Journal of Raman Spectroscopy* **1998/02/01**, *29* (2). DOI: 10.1002/(SICI)1097-4555(199802)29:2<97::AID-JRS198>3.0.CO;2-E.
(60) Alben, R. Infrared and Raman Selection Rules for Molecular and Lattice Vibrations: The Correlation Method. Society of the Sigma Xi: 1973; Vol. 61, pp 241-242.
(61) Weigang Lu; Hao Zhu; Blake Birmingham; Nolan Craft; Jonathan Hu; Kenneth Park; Zhenrong Zhang. Phase transition of individual anatase TiO_2 microcrystals with large percentage

of (001) facets: a Raman mapping and SEM study. *Physical Chemistry Chemical Physics* **2023/01/27**, *25* (4). DOI: 10.1039/D2CP04882E.
(62) Porto, S. P. S.; Fleury, P. A.; Damen, T. C. Raman Spectra of TiO_2, MgF_2, ZnF_2, FeF_2, and MnF_2. *Physical Review* **1967-02-10**, *154* (2). DOI: 10.1103/PhysRev.154.522.
(63) Balachandran, U.; Eror, N. G. Raman spectra of titanium dioxide. *Journal of solid state chemistry* **1982**, *42* (3), 276-282. DOI: 10.1016/0022-4596(82)90006-8.
(64) Boytsova, O.; Zhukova, I.; Tatarenko, A.; Shatalova, T.; Beiltiukov, A.; Eliseev, A.; Sadovnikov, A. The Anatase-to-Rutile Phase Transition in Highly Oriented Nanoparticles Array of Titania with Photocatalytic Response Changes. *Nanomaterials* **2022/12**, *12* (24). DOI: 10.3390/nano12244418.
(65) Byrne, C.; Byrne, C.; Fagan, R.; Fagan, R.; Hinder, S.; Hinder, S.; McCormack, D. E.; McCormack, D. E.; Pillai, S. C.; Pillai, S. C. New approach of modifying the anatase to rutile transition temperature in TiO2 photocatalysts. *RSC Advances* **2016/10/03**, *6* (97). DOI: 10.1039/C6RA19759K.
(66) Wang, G.; Xu, L.; Zhang, J.; Yin, T.; Han, D.; Wang, G.; Xu, L.; Zhang, J.; Yin, T.; Han, D. Enhanced Photocatalytic Activity of TiO_2 Powders (P25) via Calcination Treatment. *International Journal of Photoenergy* **2012/2/19**, *2012*. DOI: 10.1155/2012/265760.
(67) Hiremath, V.; Heo, J.; Park, H.-H.; Seo, J. G. Crystallinity swayed phase transformation and oxygen vacancy formation in TiO2 aerogel photocatalysts. *Environmental research.* **2023**, *239*, 117409. DOI: 10.1016/j.envres.2023.117409.
(68) Hooper, P. A. Melt pool temperature and cooling rates in laser powder bed fusion. *Additive manufacturing.* **2018**, *22*, 548-559. DOI: 10.1016/j.addma.2018.05.032.
(69) Guisbiers, G.; Van Overschelde, O.; Wautelet, M. Theoretical investigation of size and shape effects on the melting temperature and energy bandgap of TiO2 nanostructures. *Applied Physics Letters* **2008/03/10**, *92* (10). DOI: 10.1063/1.2897297.
(70) Papanicolaou, G. C.; Kostopoulos, V.; Kontaxis, L. C.; Kollia, E.; Kotrotsos, A. A comparative study between epoxy/Titania micro - and nanoparticulate composites thermal and mechanical behavior by means of particle–matrix interphase considerations. *Polymer Engineering & Science* **2018/07/01**, *58* (7). DOI: 10.1002/pen.24668.
(71) Le Ba, T.; Várady, Z. I.; Lukács, I. E.; Molnár, J.; Balczár, I. A.; Wongwises, S.; Szilágyi, I. M.; Le Ba, T.; Várady, Z. I.; Lukács, I. E.; et al. Experimental investigation of rheological properties and thermal conductivity of SiO2–P25 TiO2 hybrid nanofluids. *Journal of Thermal Analysis and Calorimetry 2020 146:1* **2020-07-21**, *146* (1). DOI: 10.1007/s10973-020-10022-4.
(72) Koparde, V. N.; Cummings, P. T.; Koparde, V. N.; Cummings, P. T. Sintering of titanium dioxide nanoparticles: a comparison between molecular dynamics and phenomenological modeling. *Journal of Nanoparticle Research 2007 10:7* **2008-01-10**, *10* (7). DOI: 10.1007/s11051-007-9342-3.
(73) Khairallah, S. A.; Anderson, A. T.; Rubenchik, A.; King, W. E. Laser powder-bed fusion additive manufacturing: Physics of complex melt flow and formation mechanisms of pores, spatter, and denudation zones. *Acta materialia.* **2016**, *108*, 36-45. DOI: 10.1016/j.actamat.2016.02.014.
(74) Körner, C.; Attar, E.; Heinl, P. Mesoscopic simulation of selective beam melting processes. *Journal of materials processing technology* **2011**, *211* (6), 978-987. DOI: 10.1016/j.jmatprotec.2010.12.016.
(75) Huang, X.; Gao, Y.; Yang, T.; Ren, W.; Cheng, H.-M.; Lai, T.; Huang, X.; Gao, Y.; Yang, T.; Ren, W.; et al. Quantitative Analysis of Temperature Dependence of Raman shift of monolayer WS2. *Scientific Reports 2016 6:1* **2016-08-31**, *6* (1). DOI: 10.1038/srep32236.

(76) Lan, T.; Tang, X.; Fultz, B. Phonon anharmonicity of rutile TiO_2 studied by Raman spectrometry and molecular dynamics simulations. *Physical Review B* **2012-03-27**, *85* (9). DOI: 10.1103/PhysRevB.85.094305.
(77) Szymczak, M.; Szymczak, M.; Piotrowski, W. M.; Piotrowski, W. M.; Woźny, P.; Woźny, P.; Runowski, M.; Runowski, M.; Marciniak, L.; Marciniak, L. A highly sensitive lifetime-based luminescent manometer and bi-functional pressure–temperature sensor based on a spectral shift of the R-line of Mn4+ in K2Ge4O9. *Journal of Materials Chemistry C* **2024/05/16**, *12* (19). DOI: 10.1039/D3TC04812H.
(78) Rani, C.; Rani, C.; Pathak, D. K.; Pathak, D. K.; Tanwar, M.; Tanwar, M.; Kandpal, S.; Kandpal, S.; Ghosh, T.; Ghosh, T.; et al. Anharmonicity induced faster decay of hot phonons in rutile TiO2 nanorods: a Raman spectromicroscopy study. *Materials Advances* **2022/02/07**, *3* (3). DOI: 10.1039/D1MA00940K.
(79) Baldi, A.; Askes, S. H. C. Pulsed Photothermal Heterogeneous Catalysis. *ACS Catalysis* **February 22, 2023**, *13* (5). DOI: 10.1021/acscatal.2c05435.
(80) Oldenburg, S. J. Light scattering from gold nanoshells. Ph.D., Rice University, United States-Texas, 2000.
(81) Fang, J.; Reitz, C.; Brezesinski, T.; Nemanick, E. J.; Kang, C. B.; Tolbert, S. H.; Pilon, L. Thermal Conductivity of Highly-Ordered Mesoporous Titania Thin Films from 30 to 320 K. **July 8, 2011**. DOI: 10.1021/jp203400t.
(82) Hopkins, P. E.; Mittal, M.; Phinney, L. M.; Grillet, A. M.; Furst, E. M. Ultra-low thermal conductivity of ellipsoidal TiO2 nanoparticle films. *Applied Physics Letters* **2011/09/26**, *99* (13). DOI: 10.1063/1.3644987.
(83) Carattino, A.; Caldarola, M.; Orrit, M. Gold Nanoparticles as Absolute Nanothermometers. *Nano Lett* **January 9, 2018**, *18* (2). DOI: 10.1021/acs.nanolett.7b04145.
(84) Baffou, G.; Bon, P.; Savatier, J.; Polleux, J.; Zhu, M.; Merlin, M.; Rigneault, H.; Monneret, S. Thermal Imaging of Nanostructures by Quantitative Optical Phase Analysis. *Acs Nano* **February 15, 2012**, *6* (3). DOI: 10.1021/nn2047586.
(85) Li, Y.; Zhou, K.; Tor, S. B.; Chua, C. K.; Leong, K. F. Heat transfer and phase transition in the selective laser melting process. *International journal of heat and mass transfer* **2017**, *108*, 2408-2416. DOI: 10.1016/j.ijheatmasstransfer.2017.01.093.
(86) Höfflin, D.; Sauer, C.; Schiffler, A.; Manara, J.; Hartmann, J. Pixelwise high-temperature calibration for in-situ temperature measuring in powder bed fusion of metal with laser beam. *Heliyon* **2024**, *10* (7), e28989-e28989. DOI: 10.1016/j.heliyon.2024.e28989.
(87) Lu, W.; Birmingham, B.; Voronine, D. V.; Stolpman, D.; Ambardar, S.; Erdogan, D. A.; Ozensoy, E.; Zhang, Z.; Solouki, T. From Aluminum Foil to Two-Dimensional Nanocrystals Using Ultrasonic Exfoliation. *The Journal of Physical Chemistry C* **April 2, 2021**. DOI: 10.1021/acs.jpcc.0c10935.
(88) Turkevich, J.; Turkevich, J.; Stevenson, P. C.; Stevenson, P. C.; Hillier, J.; Hillier, J. A study of the nucleation and growth processes in the synthesis of colloidal gold. *Discussions of the Faraday Society* **1951/01/01**, *11* (0). DOI: 10.1039/DF9511100055.
(89) Fitra, M.; Daut, I.; Irwanto, M.; Gomesh, N.; Irwan, Y. M. Effect of TiO2 Thickness Dye Solar Cell on Charge Generation. *Energy procedia.* **2013**, *36*, 278-286. DOI: 10.1016/j.egypro.2013.07.032.